TUDelft

Delft University of Technology

Using passive and active acoustic methods for impact damage assessment of composite structures

Saeedifar, M.; Mansvelder, Jasmijn; Mohammadi, Reza; Zarouchas, Dimitrios

Important note
To cite this publication, please use the final published version (if applicable).
Please check the document version above.

Using passive and active acoustic methods for impact damage assessment of composite structures

Milad Saeedifar[a,*], Jasmijn Mansvelder[a], Reza Mohammadi[a,b], Dimitrios Zarouchas[a]

[a] *Structural Integrity & Composites Group, Faculty of Aerospace Engineering, Delft University of Technology, The Netherlands*
[b] *Non-destructive Testing Lab, Department of Mechanical Engineering, Amirkabir University of Technology, Iran*

ABSTRACT

This study aims to use the passive and active acoustic-based health monitoring methods for impact damage assessment of composite structures. To this aim, a Carbon Fiber Reinforced Polymer (CFRP) composite plate was fabricated and subjected to a simulated low-velocity impact by performing repeated quasi-static indentation tests where a loading-unloading-reloading test profile with 5 repetitions was adopted. Two Acoustic Emission (AE) broadband sensors and a network of eight piezoelectric (PZT) sensors were attached on the composite plate surface. AE (passive method) was employed during the loading and reloading phases of the indentation tests to online monitor the critical damage occurrence and also specify the damage type while scanning of the plate with Lamb waves (active method) was done to localize the damage when the structure was unloaded. Felicity Ratio (FR) index which was calculated based on the AE data could accurately detect that critical damage occurred during the 5th loading-unloading-reloading stage when the structural integrity dropped to 60% of its initial stage. Furthermore, Lamb wave signals of central frequency 150 kHz localized the impact damage with error of 0.89 cm (3.6% error respect to the shortest dimension of the scanned area).

1. Introduction

Despite the key advantages of Fiber Reinforced Polymer (FRP) composites, they are susceptible to Barely Visible Impact Damage (BVID) under out-of-plane loadings [1,2]. This type of damage can grow internally and reach a critical size without any detectable evidence on the structure surface [3]. Low-Velocity Impact (LVI) is a common transverse load that may be applied to an aircraft structure during ground operations, take-off, cruising, or landing such as falling a tool on the fuselage skin during the maintenance process, bird strike phenomenon during airplane landing or take-off, and impact of hailstones to the fuselage skin during a hailstorm [4]. Due to the difficulties of detecting this type of damage by visual inspection, especially for dark composite materials like Carbon Fiber Reinforced Polymers (CFRPs), Non-Destructive Testing (NDT) techniques seem to be a good candidate for BVID assessment in these materials. Among several techniques, i.e. ultrasonic C-scan [5,6], active thermography [7,8], vibration and modal analyses [9,10], acoustic based methods such as Lamb waves [11–13] and Acoustic Emission (AE) have a great potential to be employed as Structural Health Monitoring (SHM) techniques which they can be permanently installed on the structure for in-situ health monitoring of the structure during its operational period.

Kumar Munian et al. [14] simulated the interaction of Lamb wave with multiple delamination in laminated composites. The results showed that the energy, wavelength and frequency of the Lamb wave may vary by changing the position of delamination through the thickness of the laminate. Ricci et al. [15] employed Lamb wave to detect debonding in a stiffened composite panel. The results showed that the group velocity of the first antisymmetric mode of Lamb wave was considerably affected by the presence of delamination in the structure and it could be used as a Damage Index (DI). Mustapha et al. [16] used Lamb wave for BVID assessment in sandwich composite panels. They used two approaches to define DI; Time Reversal (TR) method and the Lamb wave intensity reduction due to the interaction of the wave with the damage. The results showed that DI values obtained from TR method are almost half of the DI values calculated based on the intensity reduction and therefore the localization error of TR is higher than the intensity reduction method.

Some other researchers used AE as a passive acoustic-based technique for BVID assessment in laminated composites. These studies almost focused on two subjects; 1) Damage detection and classification, and 2) Damage localization. Saeedifar et al. [17,18] employed AE to detect, classify and also trace the evolution of different damage mechanisms in CFRP plates under quasi-static indentation and LVI loading

conditions. There are different approaches to localize damage in a composite plate using AE such as triangulation [19,20], delta T-mapping [21,22], multi-steps and optimizing techniques [23], etc. Most of the AE localization techniques such as triangulation need to know the material properties of the composite plate to accurately localize the damage. Although some newer methods such as delta T-mapping and multi-steps and optimizing techniques do not need to the material properties for damage localization, they have some implementation difficulties that restrict the implementation of these techniques for damage localization in anisotropic composite materials in Maintenance, Repair and Overhaul (MRO) industries. For example, delta T-mapping needs to huge numbers of data training before implementing this method for the damage localization or multi-steps and optimizing techniques need to a complicated arrangement of sensor clusters and also a time-consuming optimization process to achieve an accurate localizing result.

Therefore, each of active and passive acoustic-based methods (Lamb wave and AE techniques) has some advantages and disadvantages. For example, although Lamb wave technique can detect the regions with the highest damage probability regardless the material properties and geometry of the structure, it cannot give valuable information about the history of damage growth. This is due to the active nature of Lamb wave; i.e. Lamb wave inspection is usually performed when the structure is unloaded and therefore it does not have any information about the operation period of the structure. Combining Lamb wave with another passive NDE technique, i.e. AE, lets to move from the schedule-based to condition-based maintenance paradigm which has some advantages over the first one such as improving system reliability, increasing operational availability, and reducing the times and costs of maintenance operations [24–26]. Thus, in the present study, the active and passive acoustic methods (i.e. Lamb wave and AE) are used simultaneously to enable the SHM system to judge about the damage severity besides the damage location. This is achieved by combining the in-situ AE data recorded during the loading stage of the structure with the Lamb wave results which are obtained when the structure is unloaded.

This paper proposes a combination of active and passive acoustic-based methods for impact damage assessment of composite structures. To this aim, a CFRP composite plate was fabricated and subjected to a simulated LVI loading condition by performing some quasi-static indentation tests where a loading-unloading-reloading test profile was adopted. AE technique was employed during the loading and reloading phases to detect the critical damage occurrence and also classify different damage mechanisms while image reconstruction by Lamb wave was done to accurately locate the damage when the structure was unloaded.

2. Experimental procedures

2.1. Description of the materials

A square panel with dimensions of 500 mm × 500 mm × 2 mm were manufactured by the CFRP prepregs with the layup specified in Table 1 and cured according to the manufacturer recommended cure cycle.

2.2. PZT sensors

In order to generate uniform guided waves in all directions, circular disk PZT sensors supplied by PI Ceramic GmbH were used. The specifications of the PZT disks are reported in Table 2.

2.3. AE system

In order to in-situ record AE activities of the composite plates under loading condition, two broadband, resonant-type, and single-crystal

Table 1
The layup of CFRP composite panels.

Ply	Fiber orientation	Fiber type
P1	0/90	PW
P2	45	UD
P3	90	UD
P4	−45	UD
P5	0	UD
P6	0	UD
P7	−45	UD
P8	90	UD
P9	45	UD
P10	0/90	PW

PW: Plain Weave.
UD: Unidirectional.

Table 2
The specifications of the PZT sensors [27].

Specifications	Value	Unit
Commercial Name	PI Ceramic 000053020 with silver wrap-around electrodes	–
Material	PIC255	–
Shape	Circular disk	–
Diameter	6.50	[mm]
Thickness	0.25	[mm]
Resonance frequency	308	[kHz]

piezoelectric transducers from Vallen Systeme GmbH, AE1045S-VS900M, with two external 34 dB pre-amplifiers were utilized as the AE sensors. The optimum operating frequency range of the AE sensors was [100–900 kHz]. An AMSY-6 Vallen, 8-channel AE system with 4 parametric input channels and the maximum sampling rate of 10 MHz was used to perform the AE measurements. The threshold of the receiving AE signals and sampling rate were 40 dB and 2 MHz, respectively. The Duration Discrimination Time (DDT) and Rearm Time (RAT) were 200 μs and 400 μs, respectively. Sonotech Ultrasonic Couplant was applied between the sensor and specimen surfaces to get an appropriate acoustical coupling. The functionality of the AE sensors and the data acquisition system was checked by proceeding a pencil lead break test according to ASTM E976 standard [28].

2.4. Test methods

This section describes the preliminary tests to obtain the baseline signals for the Image Reconstruction Algorithm (IMRA) and it explains the tests that were performed to localize the damage in the sequential indentation tests.

2.4.1. Baseline test

Eight PZT sensors were attached on the top face of the composite panel in a rectangular arrangement shown in Fig. 1a.

The utilized equipment for baseline test is shown in Fig. 2. The function generator Agilent 33500B Series was employed to generate Hanning-windowed sinusoidal tone burst excitation signals with a sampling frequency of 250 MHz and a 10 V peak-to-peak amplitude. In addition, the effect of excitation frequency on the IMRA results was investigated by repeating the baseline tests for four different excited signals with the central frequencies ranging from 150 to 450 kHz in steps of 100 kHz. In order to eliminate the effect of clamping fixture and the temperature variations on the wave measurement, both of baseline and current state measurements were performed on the clamped panel at the same room temperature (see Fig. 2b).

2.4.2. Sequential indentation tests

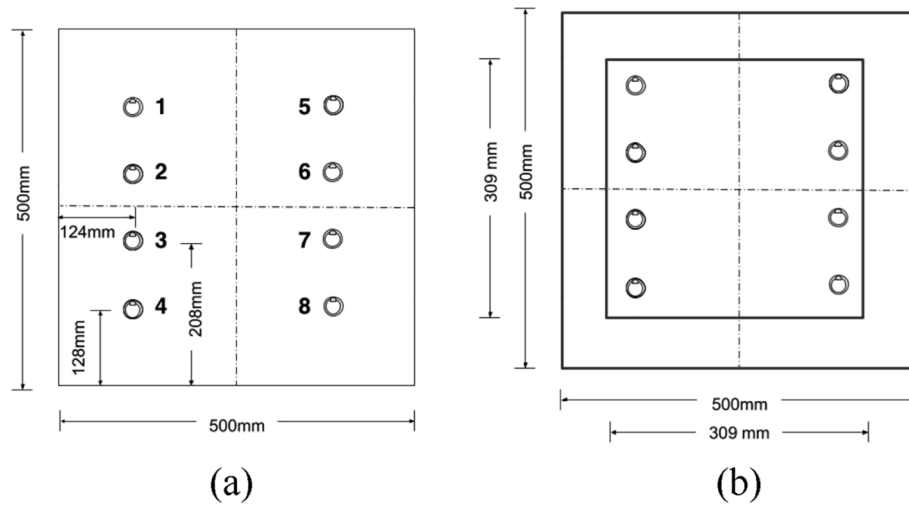Because of the quasi-static indentation tests can provide meaningful

Fig. 1. a) PZT sensors arrangement, and b) the clamped instrumented panel.

evidence of the damage events occurring during a LVI [29–30], the initiation and evolution of BVID in the scoping panel were studied using five designed sequential quasi-static indentation tests where a step-by-step increasing load (saw tooth shape) was applied to the specimens (see Fig. 3). The load is introduced by pushing a semi-spherical indenter with diameter of 37 mm by a Zwick 20 kN tensile/compression machine. The indentation load was applied under displacement control condition with the displacement rate of 2 mm/min at the position of X = 280 mm and Y = 320 mm from the specimen corner (see Fig. 4). The passive AE system was utilized to monitor the damage state during the loading stage and active PZT sensors were employed to explore the BVID location when the panel was unloaded (between two consecutive load cycles). In the loading stages, the panel was loaded up to the moment that a load drop in the force-displacement curve occurred. Then, the panel was unloaded. The maximum displacement and load for these five load cycles are presented in Table 3. The schematic and real views of the experimental indentation tests are shown in Fig. 4.

3. Image Reconstruction Algorithm (IMRA)

The proposed IMRA localizes BVID zone in the impacted panel by calculating the similarity of the recorded Lamb waves for the current state with the baseline state. IMRA contains 4 following steps:

1. Each PZT functions as an actuator while all other PZTs act as the receiver. This process is iterated for all network PZT disks in the baseline and current states.
2. DI is calculated based on the similarity between the Lamb waves of the current state and baseline (Section 3.1).
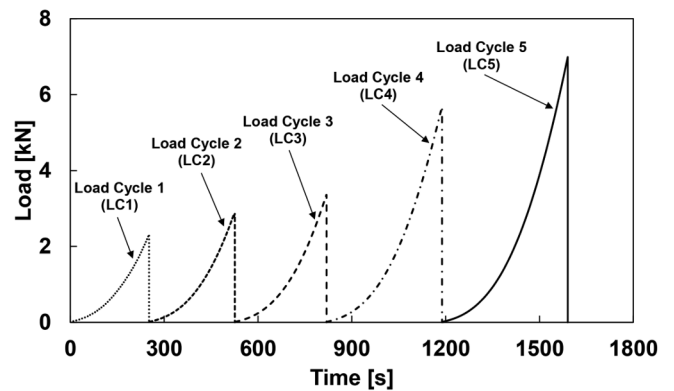3. The Pixel Influence Weight (PIW) is calculated for each actuator-

Fig. 3. The sequential increasing indentation load.

receiver pair (Section 3.2).
4. The obtained results for different actuator-receiver pairs are combined to create a damage probability contour over the inspected area (Section 3.3).

3.1. Damage index

DI is defined for each path of the PZTs network and shows the effect of damage on the desired path. Two damage indices are defined based on Pearson Correlation Coefficient (PCC) and signal energy.

3.1.1. Pearson correlation coefficient

The PCC shows the linear similarity between two signals by a real value between -1 and $+1$, which PCC of -1 shows completely
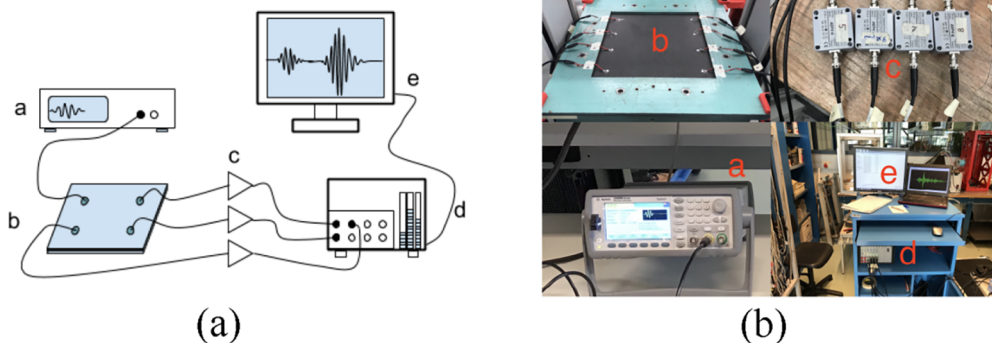

Fig. 2. a) The schematic, and b) the real view of the experimental setup for baseline tests (test apparatus description: (a) Agilent 33500B Series waveform generator, (b) panel with attached sensors, (c) preamplifiers with a gain of 34 dB, (d) Vallen AMSY-6 acoustic signal processor, and (e) laptop with Vallen Acquisition and Vallen Visual TM software).
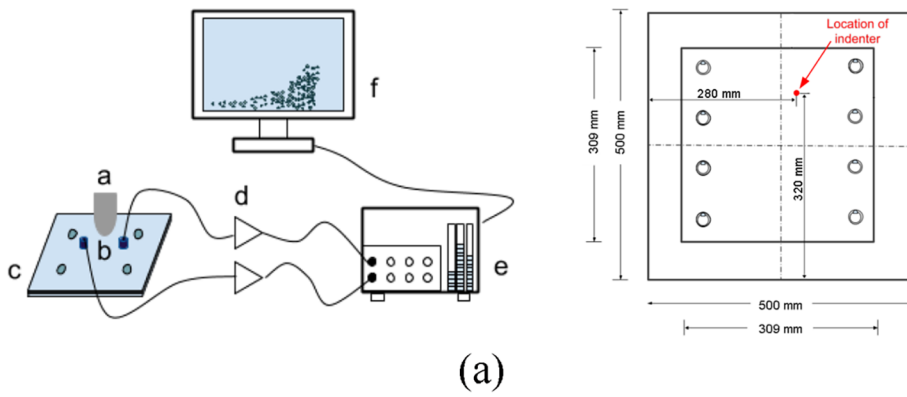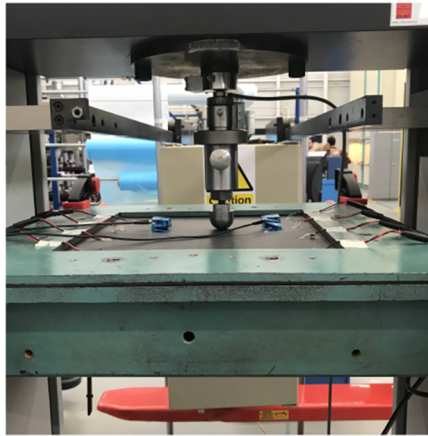
Table 3
Maximum displacement and load for different load cycles.

Load cycle	Maximum displacement [mm]	Maximum load [kN]
LC1	8.4	2.31
LC2	9.1	2.86
LC3	9.7	3.36
LC4	12.3	5.67
LC5	13.4	6.99

opposite behavior of two signals and PCC of $+1$ illustrates that two signals have completely the same trend and finally PCC of 0 shows that there is no correlation between two signals. PCC (ρ) is calculated by Eq. (1) [31]:

$$\rho = \frac{C_{BD}}{\sigma_B \sigma_D} \tag{1}$$

$$C_{BD} = \sum_{l=1}^{L} (X_B(l) - \mu_B)^2 \bullet (X_D(l) - \mu_D)^2$$

$$\sigma_B = \sqrt{\sum_{l=1}^{L} (X_B(l) - \mu_B)^2}$$

$$\sigma_D = \sqrt{\sum_{l=1}^{L} (X_D(l) - \mu_D)^2}$$

where subscripts B and D denote baseline and damaged states (current state), respectively. C_{BD} is the covariance between two the signals, σ is the standard deviation of signal, μ is the signal mean value, X is the signal samples, and L is samples number. The DI based on PCC is calculated as follows:

$$DI_{pearson} = 1 - |\rho| \tag{2}$$

$DI_{pearson}$ is varying from 0 to 1, which 0 indicates no damage state and 1 shows the highest damage probability.

3.1.2. Signal energy

A portion of the energy of a traveling Lamb wave in a damaged structure may be dissipated by the reflection and scattering of the wave due to its interaction with the damage. Thus, change in the arriving signal energy (E_D) in comparison with the baseline signal energy (E_B) can be considered as a damage indicator (DI_{energy}).

$$DI_{energy} = \frac{E_B - E_D}{E_B} \tag{3}$$

$$E_B = \sum_{n=1}^{L} (X_B(n)^2)$$

$$E_D = \sum_{n=1}^{L} (X_D(n)^2)$$

3.2. Pixel influence weight

The PIW assumes that the probability of the damage for a specific path decreases with increasing the distance from the path. This work is done by the probability ellipse. To create the probability ellipse, first, the inspected area should be meshed in x and y coordinates, according to Fig. 5(a). Then, the probability distribution forms an ellipse that the two PZT sensors act as the focal points. The effect of the damage located outside the ellipse's boundaries on the sensing path is considered zero.
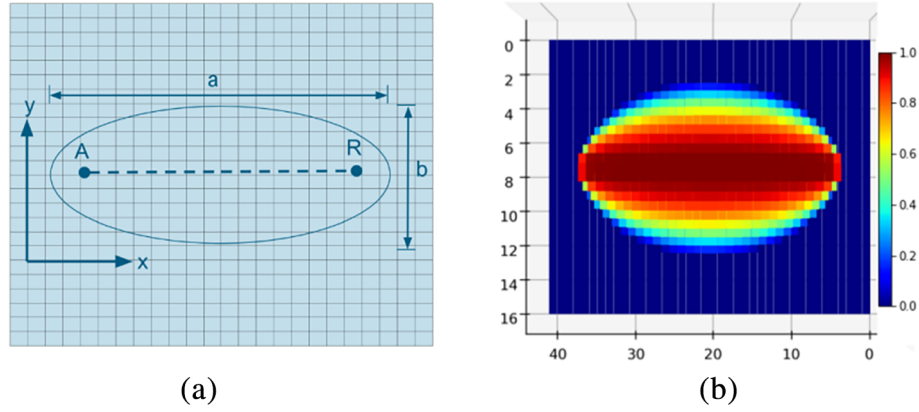
Fig. 5. a) An example of meshed area, and b) PIW distribution.

To create the probability distribution inside the ellipse, a shape factor, β, is defined so that on a straight line between the sensors, the PIW is maximum, 1, and it linearly decreases to 0 on the ellipse's boundaries.

The probability ellipse is calculated by Eq. (4). For every pixel on the grid, (x, y), first the R value is created. R indicates the ratio of the length of the major axis, a, over the distance between the two focal points, |AR|. (X_A, Y_A) and (X_R, Y_R) are the coordinates of the actuator and receiver, while (x, y) indicates the location of the pixel and S(x, y) represents the PIW [31,32].

$$R(x, y) = \frac{\sqrt{(X_A - x)^2 + (Y_A - y)^2} + \sqrt{(X_R - x)^2 + (Y_R - y)^2}}{\sqrt{(X_R - X_A)^2 + (Y_R - Y_A)^2}} \quad (4)$$

$$S(x, y) = \frac{\beta - R(x, y)}{\beta - 1}; \quad for \ \beta > R(x, y)$$

$$S(x, y) = 0; \quad for \ \beta \le R(x, y)$$

The boundaries of the ellipse are controlled by shape factor β (Eq. (5)) which is usually considered a value between 1.02 and 1.6 [33,34]. By try and error, the shape factor of 1.05 is considered for the present study.

$$a = \beta \cdot |AR|; \quad Major axis \quad (5)$$

$$b = |AR| \cdot \sqrt{\beta^2 - 1}; \quad Minor axis$$

According to Eq. (4) and Fig. 5(b), the direct path between the actuator and receiver has S(x, y) value of 1 while on the ellipse's boundaries S(x, y) value reduces to 0.

The next step in IMRA is the data fusion. The obtained DI and PIW values should be fused to create the damage probability contour over the inspected area.

3.3. Data fusion

For all the paths, the corresponding DI_{a-r} (a subscript denotes "actuator" and r subscript denotes "receiver") value is first multiplied to the corresponding $PIW_{a-r}(x, y)$ for all the pixels and then the pixel intensity ($P_{int}(x, y)$) is determined by taking the sum over all paths [31]. Fig. 6 shows the data fusion for two paths.

$$P_{int}(x, y) = \sum_{a=1}^{m} \sum_{r=1}^{n} PIW_{a-r}(x, y) \cdot DI_{a-r} \quad (6)$$

4. Results and discussions

The results are presented in two sections. First, AE results are utilized to detect the critical damage state in the specimen, then Lamb wave is employed to localize the damaged zone in the composite plate.

4.1. Critical damage detection by AE

The specimens were subjected to the five sequential indentation loads according to Section 2.4.2. The AE was used for in-situ monitoring of the induced damages in the specimens during the loading stage and Lamb wave was employed to localize the damaged zone in the specimen when it is unloaded between two consecutive load cycles. Fig. 7 shows the curves of AE amplitude and load versus time for the five load cycles. As can be seen, the considerable AE activities of load cycles 1 and 2 (LC1 and LC2) are almost initiated at the end of loading stages, while some AE activities with the amplitude lower than 60 dB are seen at the initial stage of load cycles LC3 and LC4. In addition to the aforementioned initial AE activities, another group of AE activities with the amplitude higher than 60 dB is seen at the initial stage of load cycle LC5. According to literature review [35,36], the most common damage mechanisms in laminated composites are matrix cracking,
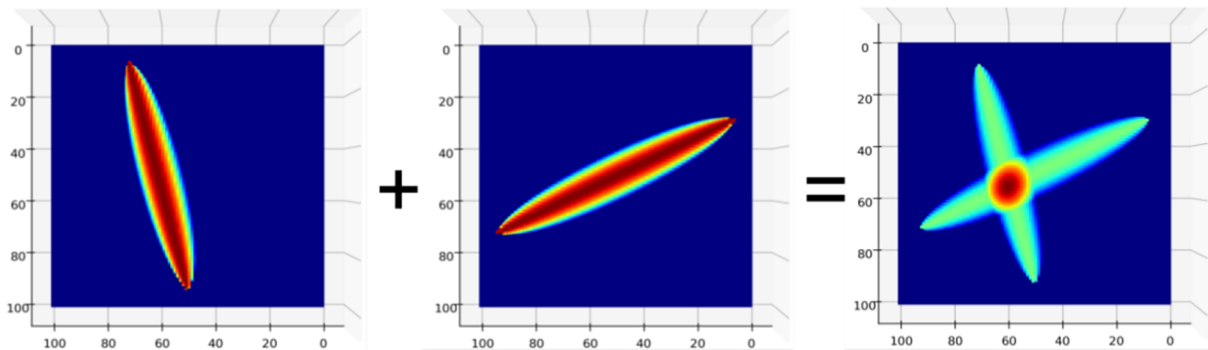

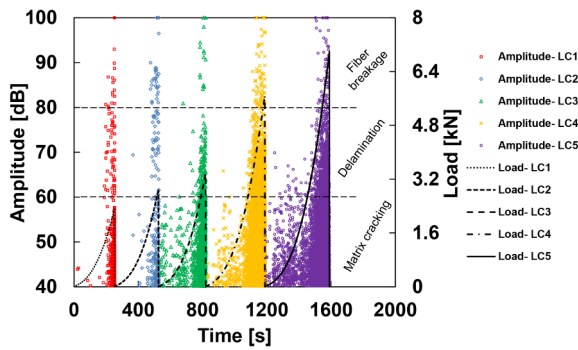**Fig. 6.** The data fusion of two paths in IMRA.

Fig. 7. AE amplitude and load versus time curves for the five load cycles.

Fig. 9. AE energy and load versus time curves for the five load cycles.

delamination, and fiber breakage and the amplitude distribution of these damage mechanisms is as follows: matrix cracking [40–60 dB], delamination [60–80 dB], and fiber breakage [80–100 dB]. Accordingly, the evolution behavior of different damage mechanisms in load cycles LC1 to LC5 can be explained. Regardless the presence of a few matrix cracks at the initial stage of load cycle LC1, a considerable number of matrix cracks and also some delamination and fiber breakages occur at the end of load cycle LC1. It is noticed to define stable and unstable damage growth. During the reloading cycle, a damage mechanism has a stable evolution behavior when the AE signal of the damage mechanism does not initiate before the maximum load of the previous loading cycle and it has an unstable evolution behavior when the AE signals of the damage mechanism initiates before the load reaches to the maximum value of the previous loading cycle. Thus, due to the fact that there is not any considerable AE activity at the initial stage of load cycle LC2, it can be concluded that all the damage mechanisms have a stable evolution behavior in load cycle LC2. Whereas, the initial matrix crack AE activities at load cycles LC3 and LC4 illustrate the fact that matrix crack has an unstable evolution behavior in these load cycles. However, due to the fact that matrix cracking is not usually considered as a critical damage mode individually [18], this point is not considered as the critical damage state of the plate. At the initial stage of load cycle LC5, some delamination AE activities are found that show the unstable behavior of delamination growth for this load cycle. Because of delamination is usually considered as the most
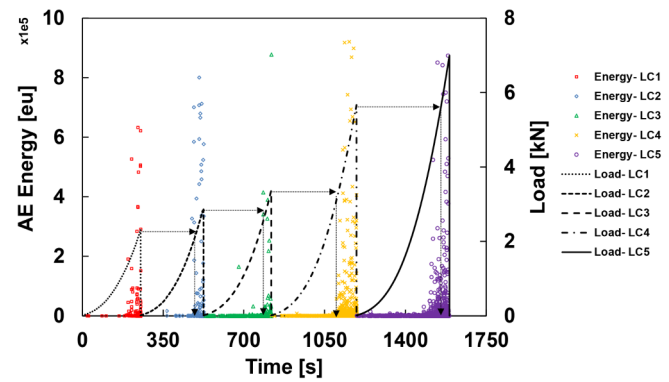
critical damage mechanism in laminated composites that may lead to catastrophic fracture of the structure, load cycle LC5 can be considered as the critical damage state of the structure. The C-scan image of the panel after load cycle LC5 is shown in Fig. 8 which a considerable damaged area is seen at the impact location. The system used to scan the panel is a Midas NDT system with Zeus software. It has one transmitter and one receiver transducers with a frequency of 10 MHz, and the specimens were placed in-between. The scanning speed used was 200 mm/min.

Fig. 9 shows AE energy and load versus time curves for the five load cycles. The maximum load of the previous load cycle and its corresponding time are illustrated on the vertical and horizontal axes. Similar to Fig. 7, the AE activities of load cycles LC1 and LC2 are initiated at the high load levels while some low energy AE activities are seen from the initial stage of loading at load cycles LC3 and LC4 which are probably related to matrix cracks. The high energy AE activities in load cycles LC3 and LC4 are initiated after the maximum load level of the previous load cycle that shows there is not a critical unstable damage growth in the material yet. However, initiation of high energy AE activities at the load levels lower than the maximum load of the previous load cycle in load cycle LC5 illustrates the presence of a critical damage with an unstable growth behavior in the material.

In order to accurately detect the critical damage occurrence and also specify the severity of damage, Kaiser and Felicity effects are employed. Kaiser effect states that the considerable AE activities during the reloading cycle for an intact structure should initiate in the proximity of the maximum load of the previous load cycle. While Felicity effect
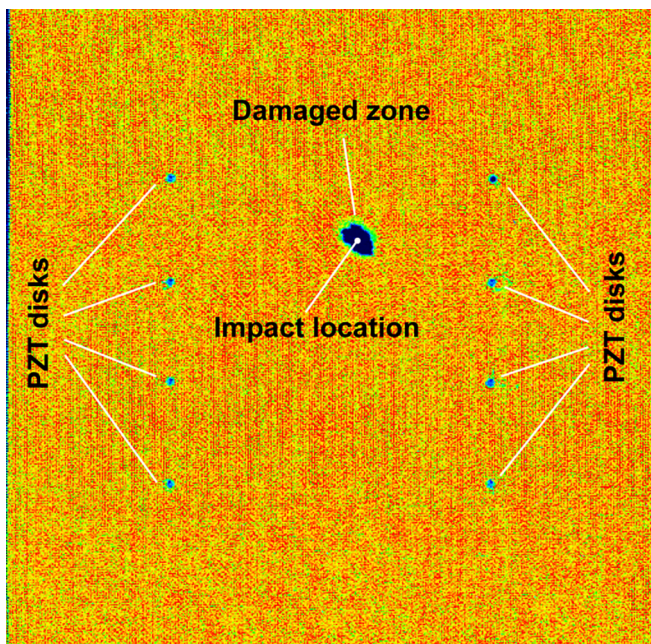

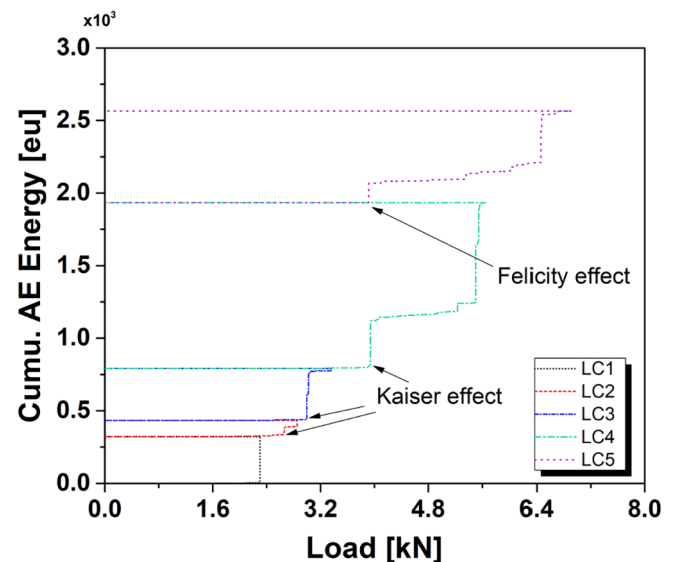**Fig. 8.** The C-scan image of the panel after load cycle LC5.

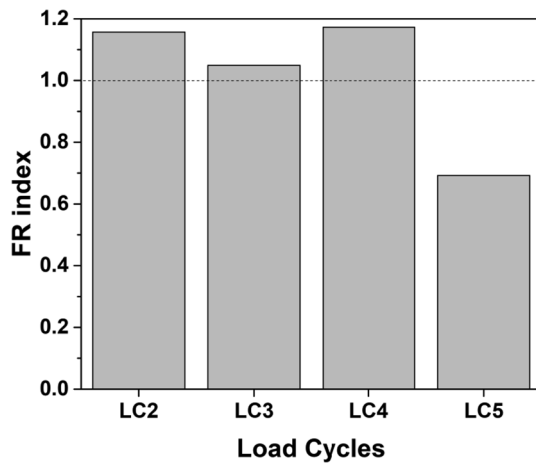**Fig. 10.** Cumulative AE energy versus load curve for the five load cycles.

Fig. 11. FR indices for load cycles LC2 to LC5.

Table 4
The damage localization error at load cycle LC4 for different excitation frequencies.

Excitation frequency (kHz)	Real impact location		$DI_{Pearson}$			DI_{Energy}		
			Predicted damage location		Error (cm)	Predicted damage location		Error (cm)
	X (cm)	Y (cm)	X (cm)	Y (cm)		X (cm)	Y (cm)	
150	28.0	32.0	28.2	31.2	0.82	29.0	31.0	1.41
250			25.2	27.2	5.56	37.6	37.2	10.92
350			28.4	20.8	11.21	23.6	25.6	7.77
450			22.4	26.4	7.92	24.0	25.6	7.55

states that observing the considerable AE activities at the load level less than the maximum load of the previous load cycle is a sign of the presence of the critical damage in the structure [37]. In order to quantify damage severity, Felicity Ratio (FR) index is defined as follows:

$$FR = \frac{P_{AE}}{P_{max}} \tag{7}$$

where P_{AE} is the corresponding load to the initiation of the considerable AE activities in the current load cycle and P_{max} is the maximum load of the previous load cycle. FR values equal or greater than 1 illustrate Kaiser effect and FR values less than 1 show Felicity effect. FR index decreases by the increase of damage severity. Fig. 10 shows cumulative AE energy versus load curve for the five load cycles. Kaiser effect can be easily seen for load cycles LC2 to LC4, while Felicity effect is obviously seen for load cycle LC5. The FR indices for load cycles LC2 to LC5 are illustrated in Fig. 11. As can be seen, the FR indices of load cycles LC2 to LC4 are larger than1, validating the Kaiser effect while FR index of load cycle LC5 is considerably less than 1 that illustrates Felicity effect.

4.2. Damage localization by Lamb wave

According to the aforementioned procedure in Section 3, Lamb wave was employed between each two consecutive load cycles to localize the damaged zone in the composite plate. In addition, the best excitation frequency of the PZT actuator should be selected to accurately localize the damage zone. To this aim, the PZT actuator was excited by four different frequencies. Fig. 12 shows the predicted damage location by the IMRA for these excitation frequencies at load cycle LC4. The real location of the impact event is shown by a circle on the images. The pixel with the highest intensity shows the predicted location of damage in each image. The localization error of the algorithm (Euclidean distance between the real impact location and the pixel with the highest intensity) for different excitation frequencies is reported in Table 4. As can be seen, increasing the excitation frequency leads to higher localization errors. This is due to the fact that the increase of the excitation frequency decreases the Lamb wave's wavelength which causes the wave to become more sensitive to smaller damage types such as intralaminar matrix cracks that subsequently leads to higher values of DI. Moreover, due to the bias induced by the algorithm during data fusion, an increase in DI leads to relatively higher pixel intensities at the center of the sensors network where the most
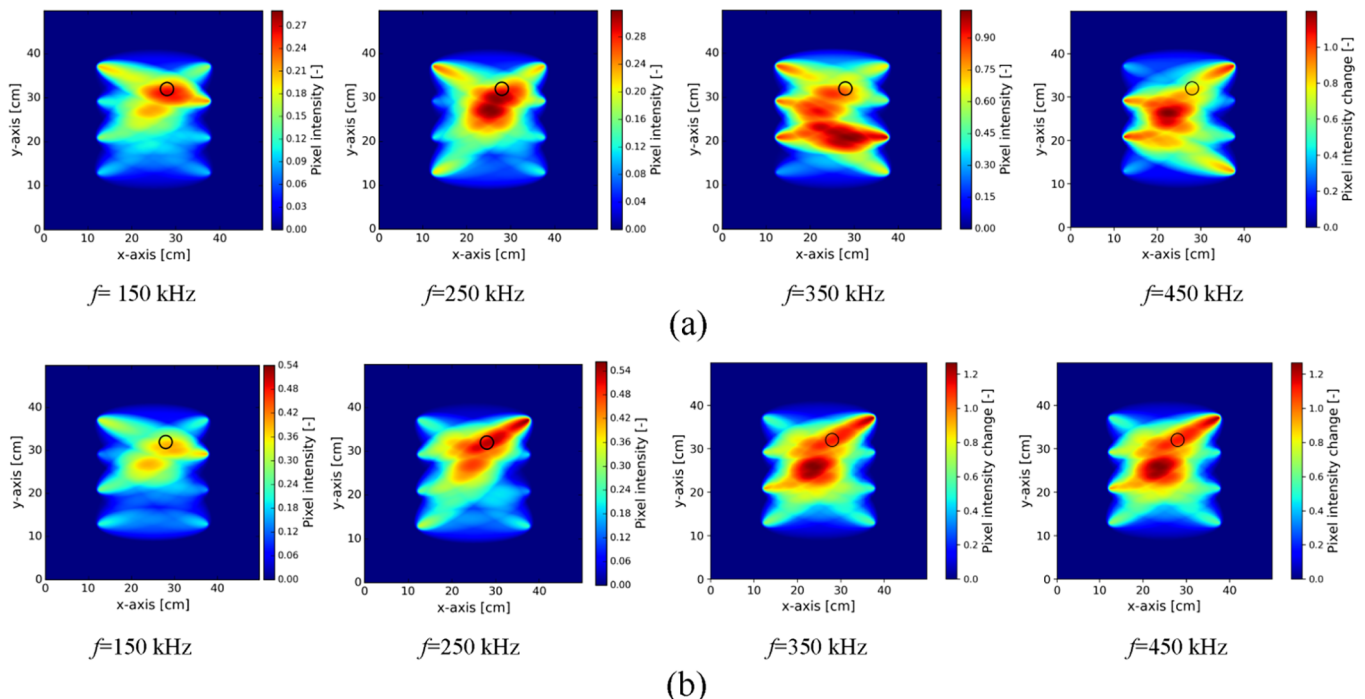

Fig. 12. Image reconstruction at load cycle LC4 for different excitation frequencies, a) $DI_{Pearson}$, and b) DI_{Energy}.
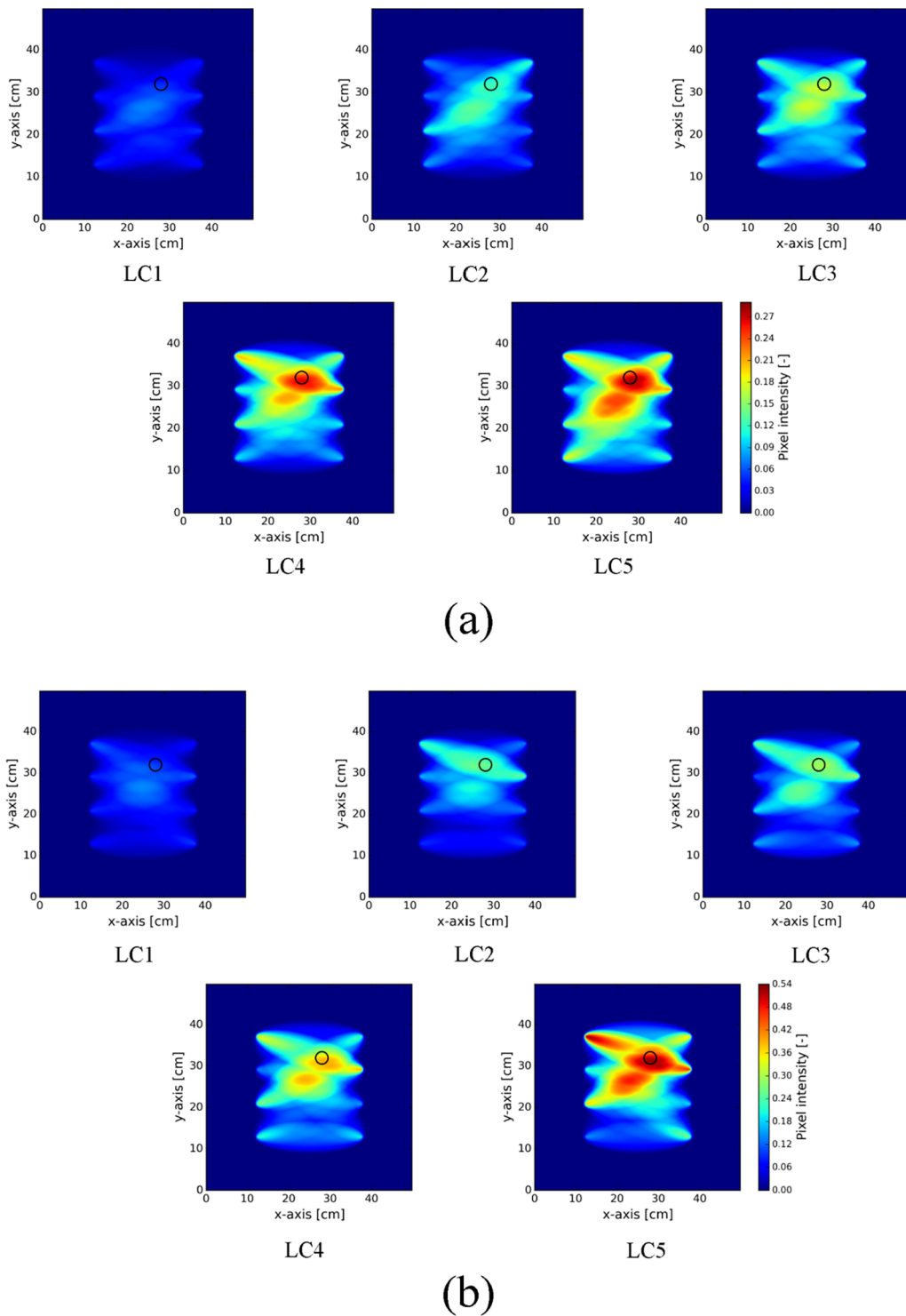
Fig. 13. Image reconstruction for the five load cycles, a) $DI_{Pearson}$, and b) DI_{Energy}.

paths will overlap. Therefore, the excitation frequency of 150 kHz was finally selected for the damage localization in load cycles LC1 to LC5.

The damage localization contours and the localization error for load cycles LC1 to LC5 are shown in Fig. 13 and Table 5, respectively. As can be seen, by increasing the applied load from load cycle LC1 to load cycle LC5, the pixel intensity rises considerably that shows the severity of damage in the material is continuously increasing. The results illustrate that DI_{Energy} and $DI_{Pearson}$ could localize the critical damage detected by AE in load cycle LC5 with the maximum localization error of 0.89 cm and 1.00 cm, respectively.

5. Conclusion

This study used the combination of passive and active acoustic-based health monitoring methods for impact damage assessment in laminated composites. A CFRP composite plate was fabricated and subjected to a sequential increasing indentation load. AE was used to in-situ detect the critical damage occurrence in the specimen during the loading stage. To this aim, FR index calculated based on the AE cumulative energy was used to identify the critical damage occurrence which is corresponded to unstable delamination growth in the material.

Table 5
The damage localization error for the five load cycles.

Load cycles	Real impact location		$DI_{Pearson}$			DI_{Energy}		
			Predicted damage location		Error (cm)	Predicted damage location		Error (cm)
	X (cm)	Y (cm)	X (cm)	Y (cm)		X (cm)	Y (cm)	
1	28.0	32.0	23.8	26.4	7.00	24.2	26.4	6.77
2			23.4	26.2	7.40	26.6	31.8	1.41
3			23.6	26.6	6.97	28.4	31.8	0.45
4			28.2	31.2	0.82	29.0	31.0	1.41
5			28.6	31.2	1.00	28.4	31.2	0.89

Lamb wave was then employed to accurately localize the damaged zone in the composite plate when the plate was unloaded between two consecutive load cycles. The proposed IMRA located the damaged zone by comparing the current state Lamb wave with the baseline Lamb wave and introducing two damage indices $DI_{Pearson}$ and DI_{Energy}. The results illustrated that DI_{Energy} has a better performance to localize the critical damage with the maximum localization error of 0.89 cm (3.6% error respect to the shortest dimension of the rectangular scanned area). Finally, this study showed that the combination of passive and active acoustic-based methods can be used for effective critical impact damage assessment in composite structures.

Data availability

The raw/processed data required to reproduce these findings cannot be shared at this time as the data also forms part of an ongoing study.

Declaration of Competing Interest

None.

Appendix A. Supplementary data

Supplementary data to this article can be found online at https://doi.org/10.1016/j.compstruct.2019.111252.

References

[1] Wagih A, Maimí P, Blanco N, et al. A quasi-static indentation test to elucidate the sequence of damage events in low velocity impacts on composite laminates. Compos A 2016;82:180–9.
[2] Tan W, Falzon BG, Chiu LNS, et al. Predicting low velocity impact damage and Compression-After-Impact (CAI) behaviour of composite laminates. Compos A 2015;71:212–26.
[3] Li N, Chen PH. Micro–macro FE modeling of damage evolution in laminated composite plates subjected to low velocity impact. Compos Struct 2016;147:111–21.
[4] Andrew JJ, Arumugam V, Santulli C. Effect of post-cure temperature and different reinforcements in adhesive bonded repair for damaged glass/epoxy composites under multiple quasi-static indentation loading. Compos Struct 2016;143:63–74.
[5] Růžek R, Lohonka R, Jironč J. Ultrasonic C-Scan and shearography NDI techniques evaluation of impact defects identification. NDT&E Int 2006;39(2):132–42.
[6] Wronkowicz A, Dragan K, Lis K. Assessment of uncertainty in damage evaluation by ultrasonic testing of composite structures. Compos Struct 2018;203:71–84.
[7] Usamentiaga R, Venegas P, Guerediaga J, et al. Automatic detection of impact damage in carbon fiber composites using active thermography. Infrared Phys Technol 2013;58:36–46.
[8] Chrysafi AP, Athanasopoulos N, Siakavellas NJ. Damage detection on composite materials with active thermography and digital image processing. Int J Therm Sci 2017;116:242–53.
[9] Katunin A. Stone impact damage identification in composite plates using modal data and quincunx wavelet analysis. Arch Civil Mech Eng 2015;15(1):251–61.
[10] Zhang Z, He M, Liu A, et al. Vibration-based assessment of delaminations in FRP composite plates. Compos B 2018;144:254–66.
[11] Diamanti K, Hodgkinson JM, Soutis C. Detection of low-velocity impact damage in composite plates using lamb waves. Struct Health Monit 2004;3(1):33–41.
[12] Kaczmarek J. Lamb wave interaction with impact-induced damage in aircraft composite: use of the A0 mode excited by air-coupled transducer. J Compos Mater 2003;37(3):217–32.
[13] Poddar B, Bijudas CR, Mitra M, et al. Damage detection in a woven-fabric composite laminate using time-reversed Lamb wave. Struct Health Monit 2012;11(5):602–12.
[14] Kumar Munian R, Mahapatra R, Gopalakrishnan S. Lamb wave interaction with composite delamination. Compos Struct 2018;206:484–98.
[15] Ricci F, Monaco E, Maio L, et al. Guided waves in a stiffened composite laminate with a delamination. Struct Health Monit 2016;15(3):351–8.
[16] Mustapha S, Ye L, Dong X, et al. Evaluation of barely visible indentation damage (BVID) in CF/EP sandwich composites using guided wave signals. Mech Syst Sig Process 2016;76–77:497–517.
[17] Saeedifar M, Ahmadi Najafabadi M, Zarouchas D, et al. Barely visible impact damage assessment in laminated composites using acoustic emission. Compos B 2018;152:180–92.
[18] Saeedifar M, Ahmadi Najafabadi M, Zarouchas D, et al. Clustering of interlaminar and intralaminar damages in laminated composites under indentation loading using acoustic emission. Compos B 2018;144:206–19.
[19] Tobias A. Acoustic emission source location in two dimensions by an array of three sensors. Non-Destr Test 1976;9:9–12.
[20] Kundu T. Acoustic source localization. Ultrasonics 2014;54(1):25–38.
[21] Eaton MJ, Pullin R, Holford KM. Acoustic emission source location in composite materials using Delta T Mapping. Compos A 2012;43(6):856–63.
[22] Pearson MR, Eaton M, Featherston C, et al. Improved acoustic emission source location during fatigue and impact events in metallic and composite structures. Struct Health Monit 2017;16(4):382–99.
[23] Kundu T, Yang X, Nakatani H. A two-step hybrid technique for accurately localizing acoustic source in anisotropic structures without knowing their material properties. Ultrasonics 2015;56:271–8.
[24] Mérigaud A, Ringwood JV. Condition-based maintenance methods for marine renewable energy. Renew Sustain Energy Rev 2016;66:53–78.
[25] Ahmad R, Kamaruddin S. An overview of time-based and condition-based maintenance in industrial application. Comput Ind Eng 2012;63(1):135–49.
[26] Eleftheroglou N, Zarouchas D, Loutas T, Alderliesten R, Benedictus R. Structural health monitoring data fusion for in-situ life prognosis of composite structures. Reliab Eng Syst Saf 2018;178:40–54.
[27] PI Ceramic GmbH. Piezoelectric discs datasheet. Germany: PI Ceramic GmbH; 2018.
[28] ASTM E976-10. Standard guide for determining the reproducibility of acoustic emission sensor response. West Conshohocken, PA: ASTM International; 2010.
[29] Sutherland LS, Guedes Soares C. The use of quasi-static testing to obtain the low-velocity impact damage resistance of marine GRP laminates. Compos B 2012;43:1459–67.
[30] Aoki Y, Suemasu H, Ishikawa T. Damage propagation in CFRP laminates subjected to low velocity impact and static indentation. Adv Compos Mater 2007;16(1):45–61.
[31] Zhao X, Gao H, Zhang G, et al. Active health monitoring of an aircraft wing with embedded piezoelectric sensor/actuator network: I. Defect detection, localization and growth monitoring. Smart Mater Struct 2007;16:1208–17.
[32] Memmolo V, Ricci F, Boffa ND, et al. Structural health monitoring in composites based on probabilistic reconstruction techniques. Procedia Eng 2016;167:48–55.
[33] De Fenza A, Petrone G, Pecora R, et al. Post-impact damage detection on a winglet structure realized in composite material. Compos Struct 2017;169:129–37.
[34] Wang D, Ye L, Lu Y, et al. Probability of the presence of damage estimated from an active sensor network in a composite panel of multiple stiffeners. Compos Sci Technol 2009;69:2054–63.
[35] Liu PF, Chu JK, Liu YL, et al. A study on the failure mechanisms of carbon fiber/epoxy composite laminates using acoustic emission. Mater Des 2012;37:228–35.
[36] Barré S, Benzeggagh ML. On the use of acoustic emission to investigate damage mechanisms in glass-fibre-reinforced polypropylene. Compos Sci Technol 1994;52:369–76.
[37] Lovejoy SC. Acoustic emission testing of beams to simulate SHM of vintage reinforced concrete deck girder highway bridges. Struct Health Monit 2008;7(4):329–46.